

# Robust data management for high through-put light sheet microscopy of whole mouse brains

M. Caroline Müllenbroich,<sup>a,b</sup> Ludovico Silvestri,<sup>a,c</sup> Leonardo Onofri,<sup>e</sup> Irene Costantini,<sup>a</sup> Marcel van 't Hoff,<sup>a,b,f</sup> Leonardo Sacconi,<sup>a,c</sup> Giulio Iannello,<sup>e</sup> Francesco S. Pavone,<sup>a,b,c,d</sup>

<sup>a</sup>European Laboratory for Non-linear Spectroscopy (LENS), University of Florence, Italy

<sup>b</sup>Department of Physics and Astronomy, University of Florence, Italy

<sup>c</sup>National Institute of Optics, National Research Council, Italy

<sup>d</sup>International Center for Computational Neurophotonics (ICON Foundation), Italy

<sup>e</sup>Integrated Research Centre, University Campus Bio-Medico of Rome, Italy

<sup>f</sup>Distrio, Amsterdam, The Netherlands

**Abstract.** 200 words limit. no numerical references presenting concisely the objectives, methodology used, results obtained, and their significance.

**Keywords:** Light sheet microscopy, big data, whole brain mounting, data management, whole brain imaging, rolling shutter, 7,8..

**Address all correspondence to:** First author, University Name, Faculty Group, Department, Street Address, City, Country, Postal Code; Tel: +1 555-555-5555; Fax: +1 555-555-5556; E-mail: [myemail@university.edu](mailto:myemail@university.edu)

## 1 Introduction

The highly ambitious project of mapping and understanding each and every neuronal connection in the whole brain has been moved from the realm of wishful longing to feasible reality by the recent advent of light sheet fluorescent microscopy (LSFM). With this technique 3D data sets can be acquired with a resolution that is high enough to identify neurons and their dendritic, axonal and spine features in time scales which are no longer the bottle neck of high-throughput acquisition. In LSFM, the sample is illuminated with a thin sheet of light confined into the focal plane of the detection objective, which collects the fluorescence emission along an axis perpendicular to the illumination plane.<sup>1</sup> This technique drastically reduces the imaging acquisition time by recording millions of pixels in parallel and affords optical sectioning by operating fluorescence excitation and detection on separate, perpendicularly oriented paths where the excitation light sheet and the detection focal plane overlap. Consequently fluorophores outside the light sheet are neither bleached nor contribute blurring out-of-focus noise. Consequently LSFM reduces phototoxicity and photo-bleaching while achieving excellent resolution at high penetration depths; however, it requires the sample to be transparent.

Several challenges remain to be overcome, however, to allow fast and, most of all systematic, production of reliable datasets and their meaningful interpretation to further our understanding of neuronal networks. Those challenges include fast, cheap and reproducible sample preparation, automated image acquisition that does not require constant attention by an expert and, most crucially, the storage, interpretation and analysis of the unprecedented huge data sets light sheet microscopy routinely produces. The mapping and understanding of this “big data” is a colossal task that requires the expertise of computer scientists to employ fully automated post-processing, for example, to do cell counting or blood vessel segmentation. On the other hand, the imaging of large, intrinsically opaque samples in light sheet microscopy necessitates clearing protocols based

on refractive index matching which render the tissue transparent. This makes LSFM a truly interdisciplinary field in which the technological advances by optical developers need to be matched by novel development in the area of information and biotechnology.

Here we will present a state-of-the-art LSFM, as it is implemented in our lab, which is especially beneficial to acquire 3D data sets of large, clarified and structurally intact mouse brains. The LSFM features double-sided illumination with a digitally scanned light sheet and a sample chamber which has been specifically designed for the the imaging of large ( $> 1\text{cm}^3$ ), immersed and freely movable samples. After briefly presenting the optical clearing protocol we employ to render our samples transparent, we explain how to prepare and mount the samples for stable, 3D imaging for several days. In addition to a full description of the optical setup, the control hardware and software, we further present a practical guide for the alignment of a LSFM, a non-trivial task that requires careful consideration. A systematic approach to handle, store and analyse the data is explained in detail. We further explain about the data volume we produce how it can be reduced and handled. The imaging capabilities are demonstrated by 3D reconstructions of biological specimens. The final sentence of the introduction needs to be amazing.

## 2 Optical path

### 2.1 Laser unit

The custom-made, confocal light sheet microscope is equipped with 5 linearly polarised, cw lasers for fluorescence excitation (Figure 1,A). The wavelengths were chosen to excite the most common fluorophores (see Table 2 for the manufacturer and specifications of opto-mechanical components). The laser light from each laser is first collimated and expanded with a telescope (f140, f200) and then combined into a common path with a beam steering mirror and a long-pass filter (Semrock, LaserMUX™ series). An acousto-optical tunable filter (AOTF) acts as fast ( $\mu\text{s}$ ) electronically tunable filter which uses the acousto-optical interaction inside an anisotropic medium to select and transmit any combination of up to four of the laser lines. The radio-frequency applied on the AOTF transducer controls the wavelength being transmitted into the first order and the radio-frequency amplitude allows to adjust the transmitted light intensity. Due its nonlinear response we measured the AOTF light transmittance for each wavelength as a function of radio frequency amplitude and determined a look-up table to linearise the output. The zero order light is blocked by an iris. An electro-optical laser modulator acts like a wave plate with electronically controlled retardation and rapidly rotates (few hundreds ns) the input polarisation of the excitation light by  $90^\circ$ . The wavelength-dependent, high voltage that needs to be applied to the birefringent crystal inside the modulator to change the optical path length is provided by a two-step pre-amplification system. First, a low voltage, analog signal from the DAQ board is pre-amplified with custom made electronics and then fed into a commercial high voltage amplifier. A digital line is used to electronically control the frequency with which the polarisation is changed. After the laser modulator the excitation beam is further expanded by a factor of two with two achromatic doublets (f100, f200).

### 2.2 Illumination unit

From here on three different light paths can be chosen through flip mirrors. One light path option guides the light through an axicon (apex angle of  $160^\circ$ ) and an achromatic doublet (f50) to create a Bessel beam. The other two options create Gaussian beams of different beam diameter. This

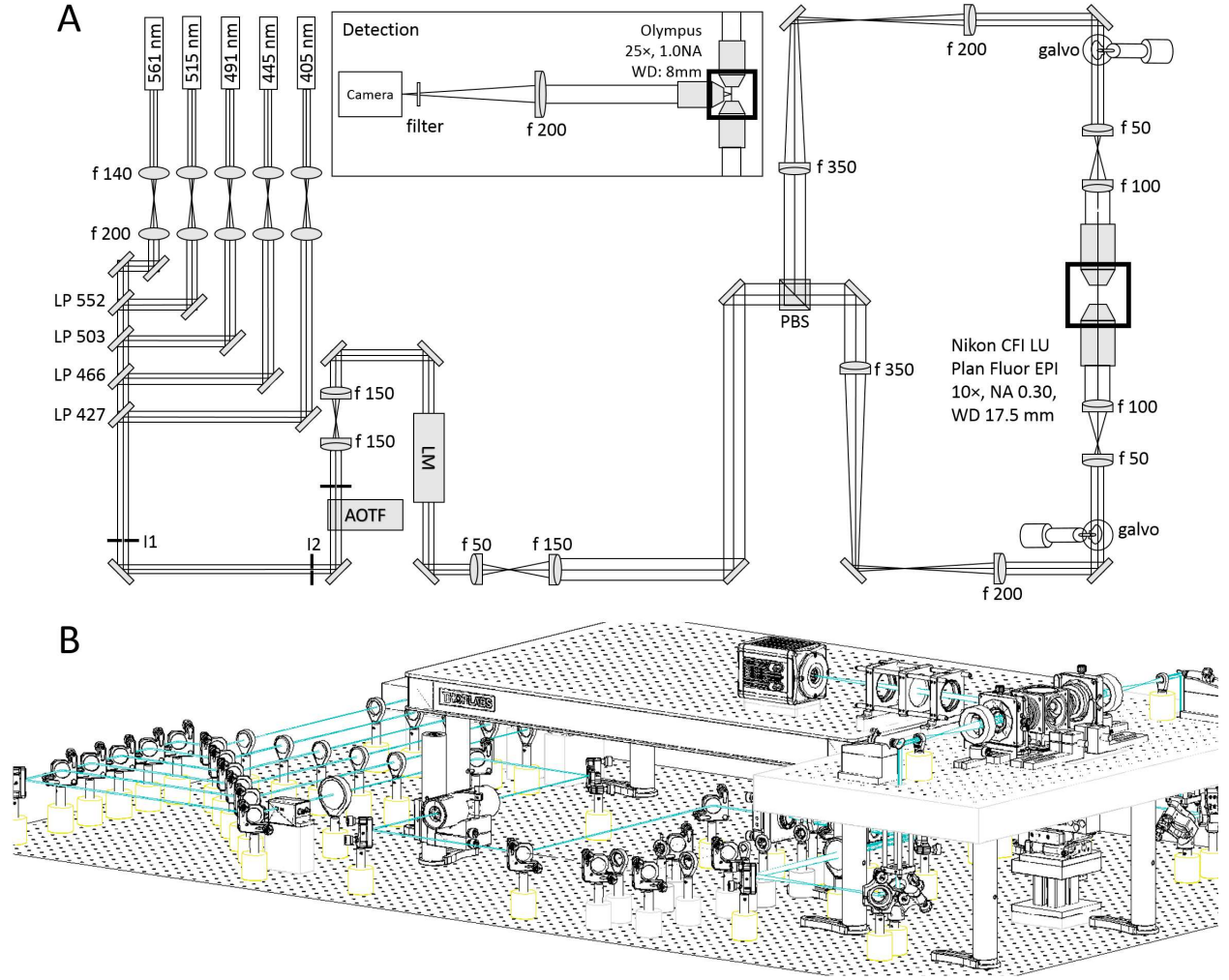


Fig 1: (A) Topview of the excitation path. The galvo scanners are mounted above periscopes. LP: long-pass filter, I: iris, AOTF: acousto-optical tunable filter, LM: laser modulator, PBS: polarisation beam splitter, ABCD: flip mirrors. Inset: detection. (B) Oblique view of the microscope. A custom-made breadboard serves to mount the sample chamber and objectives at an elevated height and features two circular holes at the edges for the periscopes and a large central cut out for the translation stages. A second breadboard is used for the camera.

diameter variation translates to different fields of view later on in the detection path. The three options are recombined before a polarising beam splitter cube which splits the excitation light depending on its polarisation into one of the two identical excitation arms. The beam is reduced with a telescope (f350, f200) whose telecentric plane coincides with the mirrored surface of a galvanometric scanner (galvo). The galvos are mounted on a custom made optical breadboard which features two circular holes to pass the periscopic beams and a large central cut-out for the sample chamber and motor stages.

The scan mirror surface is re-imaged with a telescope (f50, f100) onto the back aperture of a long working distance, low magnification objective (Nikon, 10x 0.3NA WD 17.5mm). The two excitation objectives are designed for air immersion but are immersed into the clearing solution within the sample chamber. A coverslip glued to the front housing edge serves the dual purpose of maintaining the first diffractive surface between the front optical element and the air and to protect the front lens elements from the organic solvent. The light sheet is generated digitally<sup>7,8</sup> by scanning the excitation beam across the focal plane of the detection objective. This generates incoherent illumination resulting in fewer artefacts. Additionally each line of specimen is illuminated with the same intensity creating a homogeneous light sheet which is particularly advantageous for the quantitative investigation of large samples in their entirety.

### 2.3 Detection unit

In its simplest form, the fluorescence detection unit of a light sheet microscope is a conventional wide-field microscope: an objective lens, a fluorescent filter and a tube lens for an image on a wide-field detector. Fluorescence is collected with an objective that is specifically designed for immersion in clearing solutions. The objective is equipped with a correction collar allowing for immersion in media with refractive indices ranging from 1.41 to 1.52 (Olympus, XLSLPLN25XGMP). To image the whole volume of interest the objective has a relatively low magnification of 25x and a large working distance of 8mm yet a high numerical aperture (1.0NA) affords high resolution imaging. A tube lens of 200mm creates the primary image on a sCMOS camera (Orca Flash4.0, Hamamatsu) with a chip of over 4 megapixels. In contrast to CCD sensors each pixel of a sCMOS camera sensor has a separate photodetector and amplification unit which means that sCMOS pixels can be read out independently from each other. The cell size of the OrcaFlash is  $p^2 = 6.5\mu\text{m} \times 6.5\mu\text{m}$  over an active area of 13.3mm. With a 200mm tube lens the field of view in the sample is  $480\mu\text{m}$ .

In the rolling shutter data acquisition mode only a subset of adjacent horizontal pixel lines is simultaneously exposed and this active detection region is moved across the image sensor. With the delay between the exposure of two adjacent lines set to the minimum time required to read out a single line ( $t = 9.7\mu\text{s}$ , see Table 3) the entire frame of 2048 horizontal lines is activated within 19.86ms. Setting the line exposure time to  $l = 3\text{ms}$  results in approx.  $k = l/t \approx 300$  lines being simultaneously exposed at any time. This detection area is swept from the top to the bottom of the chip and acts like a moving, virtual confocal slit corresponding to a width of  $d_s = kp/M_{\text{eff}} = 0.72\text{m}$  in the sample space. With the given values of line exposure and line read out time, the camera acquires images at a frame rate of  $\nu = 1/(2048t+l) \approx 44\text{Hz}$ .

The camera was run as master in the internal trigger mode and a synchronisation pulse generated with the exposure of each new line was used as an output trigger for a data acquisition and generation device (DAQ) from National Instruments which was operated as slave. The saw-tooth

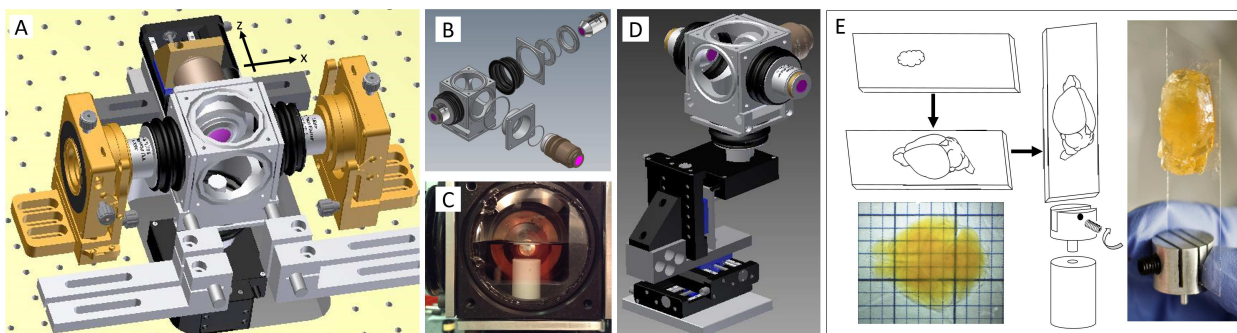


Fig 2: Schematic of light sheet microscopy. (A) Fluorescence excitation (along x axis) and detection (along z axis) are operated on independent, perpendicular light paths where the excitation light sheet and the detection focal plane overlap. (B) The custom-made sample chamber is assembled with silicone bellows and seal rings. The clarified, fluorescently-labelled brain is mounted on a Teflon cylinder in the centre of the watertight chamber (C) and can be translated and rotated freely with piezo motors (D). (E) Mounting of a clarified, fluorescently labelled brain. The brain is glued onto a coverslip and inserted into an adapter that slides into the Teflon cylinder.

driving signal for the galvo mirrors was generated by the DAQ and synchronised with the pixel line reset pulses from the camera to achieve confocal line detection.<sup>9</sup> For optimal imaging it is crucial that the sample-emitted line of fluorescence is in the centre of the rolling shutter at the start of each image acquisition and furthermore travels with the same speed during stack acquisition. Any deviation from precise synchronisation results in image artefacts and severely degraded image contrast. The confocal resolution can be changed at run-time by changing the user-defined line exposure time and with it rolling shutter width, that is the number of horizontal pixel lines simultaneously exposed.

### 3 Sample mounting and motion

To elucidate neuronal projections and functional connections in structurally intact tissue it is paramount to be able to image centimeter-sized, clarified samples, such as mouse brains, with high resolution in whole mount preparation. While promising clearing protocols are well documented in literature,<sup>2,3</sup> the question of sample preparation and mounting in light sheet microscopy is not trivial but requires novel approaches to such extent that it is becoming a separate field of research and very diverse strategies such as FEP tubes, 3D printed chambers and Quartz cuvettes have been reported,<sup>3-6</sup> however, these approaches are limited to much smaller sample volumes. The problem of sample mounting in a light sheet microscope arises from the fact that optical access to the sample is required from 3-4 planar sides leaving only two opposing sides to insert, fix and move the sample. Most commonly the vertical direction is chosen. Stable mounting is hereby a key concern as a whole brain tomography can require image acquisition in excess of 24 hours and the effects of gravity, tissue shrinking/expansion and evaporation of the clearing solution over such time spans might have to be considered.

For the acquisition of whole brain data sets, we fix a clarified and fluorescently-labelled mouse brain with super glue to a coverslip (Figure 2,D). The brain is oriented along its axial orientation with the olfactory bulbs at the top and the cerebellum at the bottom of the coverslip. The coverslip



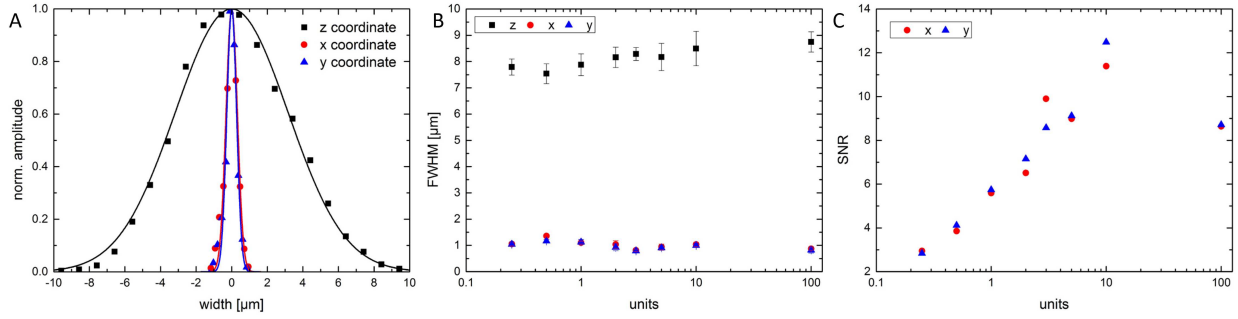


Fig 3: Optical characterisation. (A) Exemplary lateral and axial intensity profiles of sub-resolution beads and fits to Gaussian. (B) For each unit 10 bead profiles were fitted in all three dimensions and their FWHM was averaged. (C) The signal to noise ratio.

is slid into a bottom adaptor and tightened with a plastic-capped grub screw. The bottom adaptor is inserted into a Teflon cylinder with the coverslip being positioned on the far side of the detection objective. Three different slits in the adapter correspond to varying distances to the detection objective and give variability in sample thickness for example to allow also for the mounting of rat brain hemispheres.

We designed a cubic, water-tight sample chamber (Figure 2, A) that allows access from all six sides while maintaining the 3D integrity of large, clarified and fluorescently-labelled mouse brains. The sample chamber is tightly bolted to the optical breadboard while soft connections using silicone bellows allow for adjustable movements of the objectives and free 3D motion of the motor stages (Figure 2, B). All connections are sealed with rubber rings and silicone caulk and additionally tightened with cable binders. In this way the objectives can be refocused and realigned without compromising the watertight seal of the chamber (Figure 2, C). The clarified brains are imaged immersed in clearing solution composed of 63% TDE in Phosphate buffered saline (PBS) and a refractive index of 1.45. To fill the entire volume of the sample chamber approximately 400ml clearing solution are needed. A motorized x-, y-, z-,  $\theta$ -stage (Physik Instrumente, see Table 2) allows free 3D motion and rotation of the Teflon cylinder which reaches into the centre of the chamber (Figure 2, D). Illumination and detection axes are horizontal and the sampler rotation occurs around the vertical axis.

## 4 Optical characterisation

An overview of imaging properties and derived quantities is given in Table 3.

## 5 Microscope management software

### 5.1 General design principles

The many components of the microscope (camera, lasers, AOTF, stages, etc.) are orchestrated together and operated through a custom-made software. Since the microscope should work mainly without human intervention for many hours (a whole-brain tomography can last a couple of days) without losing proper synchronization, software design is not a secondary issue when building a light sheet microscope for whole-brain imaging. The overall architecture of the software and its practical implementation were chosen to satisfy several principles:

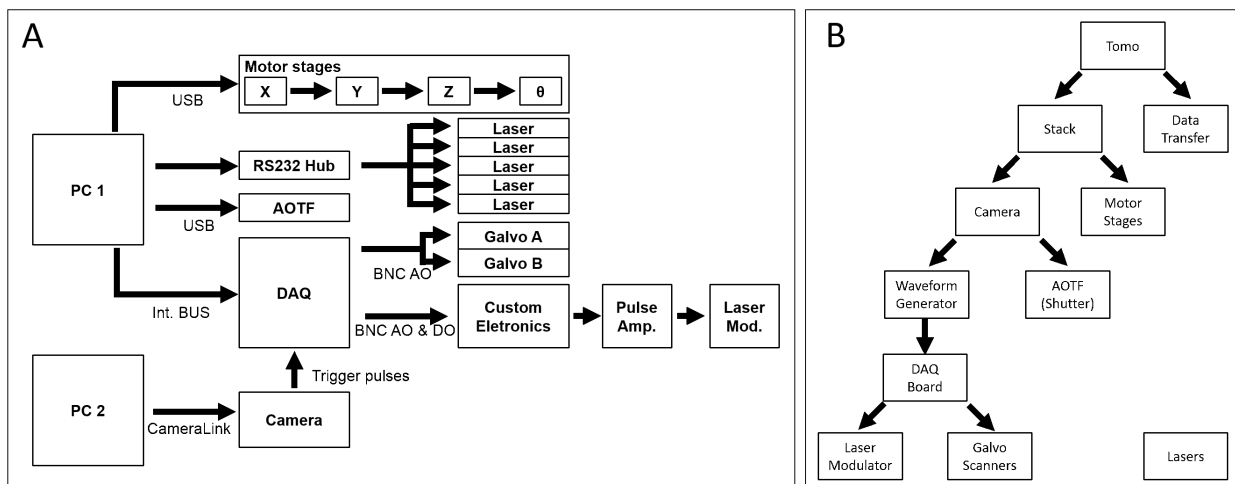


Fig 4: Schematic views of the hardware (A) and software (B) architectures of the microscope, showing physical and logical connections, respectively. The software architecture scheme clarifies the hierarchic structure of the Murmex components. AO analog output, DO digital output, DI digital input.

- *User-friendliness.* The light sheet microscope here presented was designed and developed by optical technology specialists yet needs to be operational in a multi-user environment. The greatest challenge therefore consists in making the use of the microscope easy and intuitive such that no formidable expertise is needed when it is operated by researchers with no expertise in optics and/or software development.
- *Working in a distributed environment.* The apparatus should deal with many independent hardware components, and with several data streams (see below). Individual processing steps and/or data transfer can be computationally intensive, and may need to be distributed over several computers to perform properly at run-time.
- *Robustness and ease of maintenance.* Any kind of hardware problem, from timing delay to real failure, must be automatically handled to avoid loss of precious data. Furthermore, developers must be able to fix existing code or to develop new one without having to change the whole software.
- *Reusability and scalability.* When a second or third microscope with basic similarity yet slightly specialised equipment is being designed in the same or in other laboratories, re-writing all the code from scratch is pure loss of time. Writing well structured, scalable and easily maintainable scientific software can help avoiding redundancy and boosting up productivity.

Our microscope management software has been written in LabVIEW (National Instruments, Austin, US), as this language is particularly well suited for hardware control and data acquisition through pre-developed methods. An object-oriented programming framework<sup>13</sup> has been used, dividing the entire project into well-defined self-contained modules. This framework, besides helping defining the proper scope of each software component, guarantees robustness, ease of main-

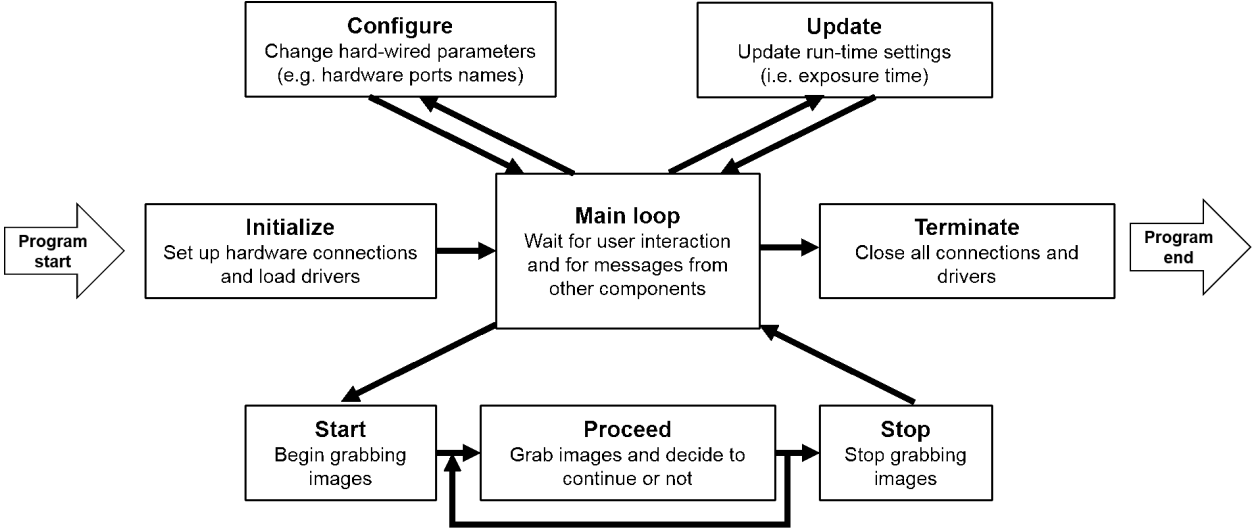


Fig 5: This graph needs a caption.

tenance, scalability and reusability. Code is stored on GitHub ([www.github.org](http://www.github.org)) to help multiple users developing software simultaneously. The graphical user interface (GUI) provides intuitive control of the apparatus as well as deep personalization. In general, the instrument parameters are already set to optimal values stored on disk, and on-line tips on how to set or change the various settings are provided. Both GUIs and code are developed according to the LabVIEW Style Guide.<sup>16</sup>

## 5.2 Murmex

To let the software operate efficiently and synchronously on different machines, the [Murmex](#) software development kit was used. This kit integrates the object-oriented programming paradigm with a messaging system, and can be used to create communicating yet independent software modules within a standardized programming scheme.

Basically, Murmex creates distributed finite state machines. These are design patterns in which one component proceed from one particular state to another based on the message it receives either from itself or from other components. For sending and receiving messages, Murmex uses the library [LabbitMQ](#), which is a wrapper of [RabbitMQ](#), a message-oriented middleware facilitating message shipment and receipt. These layers of abstraction are mostly hidden for the developers. The RabbitMQ server (message broker) needs to be installed either locally or somewhere in the network. The message-based communication allows for buffered, asynchronous and reliable message communication between several software components. Messages are routed by the broker to the specific software component by its ID. The LabbitMQ wrapper allows use of RabbitMQ inside the LabVIEW programming environment.

Murmex design pattern has twelve pre-defined common states (Initialise, Configure, Start, Stop, Proceed, Update, Reset, Inspect, Inform, Acknowledge, Fetch, Terminate) and a generic state for implementing custom states. Usually, just a few of this states are actually used in standard application. An example of a standard implementation of the Murmex state machine for a scanning system is shown in Fig. BLABLA. Each Murmex component streams information about



its current status to its 'observers', other components specified in its configuration file. Using this observer/observee hierarchy, it is possible to design large and complex network of different components, running on whatsoever number of computers connected through a local connection or the Internet. A special component, named ServiceManager (also based on Murmex), which must be running on each computer, can start executables remotely. This allows the user to start up a sophisticated configuration with multiple components executed on different computers, but steered from one computer.

### 5.3 *System timing and software organization*

A schematic overview of the hardware and software architecture of our light sheet microscope is shown in Fig. BLABLA, respectively. One personal computer (Precision T5600, Dell, Round Rock, USA) controls all the remote hardware components with the exception of the camera, which is controlled by a second, dedicated computer (Precision T7500, Dell, Round Rock, USA) to handle and manage the enormous streams of data produced (see next section). Various instrumentations are addressed either through computer ports (as USB, RS232 and CameraLink) or via analog and/or digital signals generated by a DAQ board (NI PCIe-6353, National Instruments, Austin, USA).

Synchronization of the camera rolling shutter to the scanning of the light sheet is achieved by letting the camera acquiring in free-run mode, and using a trigger output from the camera itself to time the generation of the waveforms sent to the galvo drivers. In particular, the HSYNC signal from the camera is used, providing a true-type-logic (TTL) pulse everytime the rolling shutter steps from one line to the next one. This trigger signal is used as a clock by the DAQ board, so that the line producing the light sheet moves step by step with the rolling shutter. The same HSYNC signal is used to trigger the DAQ digital signal sent to the electro-optic laser modulator. In this case, since at each position of the scanning line the modulator should go through at least two states (vertical polarization and horizontal polarization), HSYNC is used as a trigger while the clock used is the (much faster) internal clock of the DAQ board.

Each hardware component (AOTF, galvo scanners, electro-optical modulator, sample stages, camera, lasers) is managed through its own Murmex component. Since the galvo scanners and the electro-optical modulator are not addressed directly, but via analog and digital signals generated by the DAQ board, their software component just send analog and digital waveforms to an additional intermediate component responsible for DAQ board management. Beyond hardware-related software, two additional Murmex components (named Stack and Tomo) orchestrate the operation of the entire system.

The stack component is used to acquire single image stacks along the  $z$  direction, and to this aim send specific messages to coordinate the Camera and the Stages components. Stacks are collected by moving continuously the sample along  $z$  while keeping the camera acquiring in free run. The translation speed is such that in the time needed to collect a single frame the specimen has moved by a  $z$  step specified in the GUI. The Camera component uses low-level libraries from Hamamatsu to save the data, producing one single *.cxd* file (which is a proprietary tiff-like format from Hamamatsu) for each image stack. The name of this file and the path to it is specified by the Stack component.

The tomo component is used to image the entire sample by collecting many adjacent, parallel, partially-overlapping stacks. To this aim it exchanges messages with the Stack and the Stages

components. The user can specify the volume to be imaged either by inserting the maximum  $x$ ,  $y$  and  $z$  coordinates of a parallelepiped, or by providing a text file with the list of stacks to be collected ( $x$  and  $y$  coordinates, starting and ending  $zs$ ). The Tomo component also inform the experimenter about the state of the acquisition by sending an email when it's finished or if any trouble is experienced.

All the software described here can be freely downloaded from [GitHub](#). Beacuse of its modular structure and of the extensive documentation, it can be easily integrated and adapted in other microscopy systems.

## 6 Data Management

The volume of a mouse brain have been estimated from MRI measurements<sup>15</sup> as  $\simeq 0.5 \text{ cm}^3$ ; the same Authors find out that a parallelepiped encompassing the whole brain would have a volume of  $\simeq 0.9 \text{ cm}^3$ . Given the pixel size of the camera and the magnification of the system, and assuming a  $z$  step of  $2 \text{ }\mu\text{m}$ , the voxel size results  $0.234 \times 0.234 \times 2 \text{ }\mu\text{m}^3$ . This means that a mouse brain will be represented with about 4.6 TeraVoxels, while a parallelepiped encompassing the brain will result in 8.2 TeraVoxels. Since the camera produces 16 bit images with no compression, each raw voxel occupies 2 bytes of disk space, resulting in 8.3 TB for the whole brain "alone" and 14.8 TB for the parallelepiped (see Table XXXX). However, image stacks are acquired with a 10% of linear superposition, which is used later for image stitching. This redundancy expands the size of raw data to 10.2 TB and 18.3 TB, respectively.

This unprecedented amount of data challenges to the traditional way we interact with our data. Having far passed the point of taking your data home with you on a hard drive at the end of the experiment, data management in light sheet microscopy requires the development of a robust data management infrastructure, and of novel software tools to process the images in order to extract meaningful information.

### 6.1 Data handling and storage

The camera used in our light sheet microscope (Hamamatsu Orca Flash 4.0 v2) flushes the datastream directly to a dedicated workstation with 12 solid-state drives (SSD) operating in RAID 0 configuration, resulting in a virtual drive of 10.9 TB. Although this is already a large and expensive system for the current SSD technology, it is way smaller than the size of the raw datasets produced in each tomography. We thus connected the workstation to a larger network area storage (NAS) via a 10 Gbit/s network copper cable. The NAS operates in a safer data modality (RAID 5) with 32.4 TB of useful disk space. The NAS is then connected by a dedicated 10 Gbit/s link provided by the Consortium GARR (the Public Institution managing research networks in Italy) to CINECA (the main italian supercomputing center). The data flow scheme is summarized in Figure 6.

While transferring the data from the SSD to the NAS, we also perform a file conversion from the proprietary Hamamatsu format to a more manageable one. We chose the TIFF format among the others because it permits to store 3D image with lossless compression in a single file. Furthermore, it is a flexible and platform-independent format supported by numerous image processing applications. We thus developed a conversion module that leverages the functionalities offered by the interface of the DCIMGAPI library, supplied by Hamamatsu, and the freely available LibTIFF library. The module reads a single .cxd 3D image and writes it in a variable number of multi-page

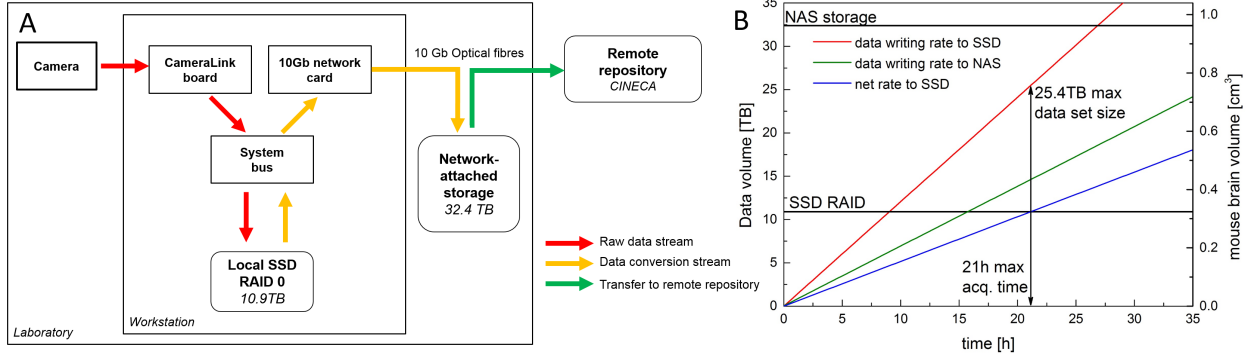


Fig 6: Scheme of the data flow. (A) Data streaming on the microscope. SSD: solid-state disk, RAID: redundant array of independent disks, NAS: network-attached storage. (B) Data production rate versus data conversion rate showing the maximum acquisition time and tomography size feasible before the SSD are filled up.

TIFF files, depending on the user-defined limit of pages per file. Since the output of the Hamamatsu camera may exceed tens of Gbytes, the image in proprietary format is read slice by slice to minimize memory requirements. The module has also an option to downsample the image on save the input image at full or reduced resolution, in order to adapt to storage availability. Usually we downsample the image in the XY plane by a factor 2 and leave the Z sampling as usual. This kind of downsampling, in combination with the lossless compression offered by the TIFF format, reduces data size by about one order of magnitude. Thus the parallelepiped volume containing the whole mouse brain can be represented using about 2-3 TB of disk space.

Although file conversion drastically reduces data size, in the current implementation it is quite slower than data production. The Camera component flushes data on the SSD with a rate  $R_{data}$  dependent on frame rate  $R_{frame}$  and on the image size:

$$R_{data}[\text{Bytes}] = 2 \times R_{frame} \times \#_{pixels}, \quad (1)$$

where the factor takes into account the 16 bit grey depth of images. The volumetric imaging rate is given by  $R_{volume} = 0.5 R_{data} \times \text{Voxel size}$ .

With a standard image size of  $2048 \times 2048$  pixels, and  $R_{frame} = 44$  Hz, data are produced at a rate  $R_{data} = 352 \text{ MB/s} \approx 1.2 \text{ TB/h}$ , which results in a volumetric rate  $R_{volume} \approx 2 \times 10^7 \mu\text{m}^3/\text{s} \approx 0.07 \text{ cm}^3/\text{h}$ . The conversion module can empty the SSD with an average rate of about 0.7 TB/h, meaning that the SSD is actually filled up during imaging at a rate of about 0.5 TB/h. Imaging sessions should thus be shorter than 21.8 hours: this limits the maximum amount of raw data being acquired continuously to approximately 25.4 TB. This is well above the disk space needed to image the parallelepiped volume encompassing a whole mouse brain. Larger specimens, as rat brain or portion of human brain, must be imaged in consecutive session until faster strategies for image conversion are devised.

## 6.2 Stitching and visualisation

Given the limited field of view of the microscope, the acquisition of macroscopic specimens required many parallel image stacks to cover all the volume. Thus, in order to achieve a 3D image of

Table 1: Data production rates with two python scripts running in parallel.

frame rate	44	Hz
size of 1 frame	8	MB
frames per stack	3900	
size of original stack	30.4	GB
size of converted stack	3	GB
stack acquisition time	88.6	s
stack conversion time	140	s
time ratio conversion/ acquisition	1.6	
data production rate	+1.2	TB/h
data conversion rate	-0.7	TB/h
net rate	+0.5	TB/h
SSD RAID	10.9	TB
max acquisition time to fill up SSDs	21	h
max tomo size to fill up SSDs	25.4	TB

the whole specimen from raw data, the Terastitcher<sup>12</sup> has been recently proposed, i.e. a stitching tool capable to deal with teravoxel-sized images. However, the Terastitcher does not support input data acquired through the serial sectioning procedure, which leads to a specimen partitioned in different layers. Furthermore, only single channel images can be processed. For these reasons, we extended the Terastitcher functionalities introducing the two following additional features: i) stitching of a specimen partitioned in a number of overlapping layers for the hippocampus reconstruction and, ii) coping with images containing more than one channel for the human brain tomography. With respect to the first requirement, that is allowing a complete reconstruction of a multi-layered raw data, we schematically depicts in Fig.1 the adopted strategy. First of all, the various input layers, each of which is composed of several parallel overlapping stacks, are separately stitched by using the existing Terastitcher tool. After this preliminary step, leveraging the layer coordinates provided by the instrument, we import the processed layers as a new volume where each layer has a partial overlap with adjacent layers. Furthermore, each layer is organized in a non-overlapping tiled format, enabling the application of a multi MIP-NCC approach,<sup>12</sup> which computes the displacement between two adjacent layers along all of the three directions (Fig. 1). When a displacement computation for each pair of adjacent layers has been computed, the overlapping regions are merged through a blending procedure which smooths the transition between layers, resembling once more the procedure used by Terastitcher for combining adjacent stacks. Finally, we note that due to the repositioning of each layer, the volume containing the reconstructed specimen might contain empty regions, which are thereby filled with black voxels. Turning our attention to the second additional feature, that is handling multi-channel images, the Terastitcher has been extended so that the MIP-NCC algorithm used for displacement computation can work on an image, which can be either the fusion of the input channels or one of the input channels. This permits to privilege the channel with more information content over the other channels as well as discard noisy channels. Note that the reconstructed 3D image can be produced with the same channel composition of raw data.

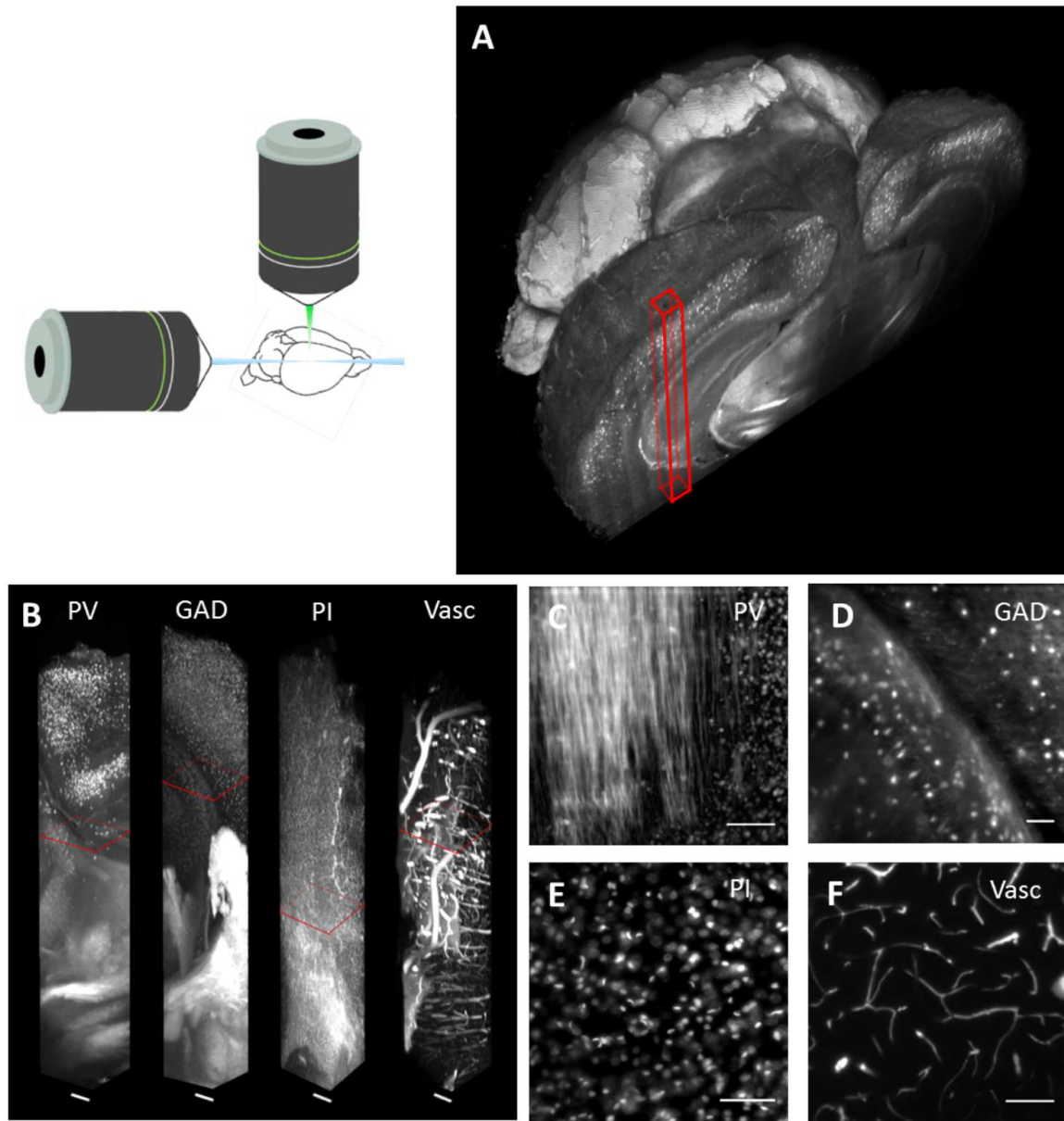


Fig 7: Whole mouse brain tomography. Imaging of whole transgenic mouse brains treated with CLARITY and cleared with TDE 63% imaged with LSM (Olympus, 25X objective). (A) 3D rendering of a parvalbumin-dTomato brain. (B) 3D rendering of stacks from PV-dTomato mouse brain, GAD-dTomato mouse brain, PI stained mouse brain, FITC-albumin labeled mouse brain, scale bar = 400 m. (C,D,E,F) High resolution insert, of the stack corresponding to red boxes in C. Scale bar = 100 m.



## 7 Data

Everybody take a look at Figure7 because it is the best we have.

## 8 Conclusion

summary Light sheet microscopy has already been a game changer for large-scale imaging by yielding data with a combination of unprecedented spatio-temporal scale. The impact of this unique measurement technique will continue to revolutionise the field of whole brain connectomics due to its ability to record millions of images over the course of days or even weeks. The data produced in this fashion easily amounts several TB per data set and needs to be stored, transferred, retrieved, processed and visualised necessitating the concurrent development of novel computational interface and analysis methods. The latter need to be robust, standardised and fully automated processes yet allow for flexible, exploratory and tailored analysis.

## 9 Outlook

where are we going next with this? ask Leo Onofri and Giulio to contribute to this, issues data mangament, aberration correction mapping of complementary data sets obtained in the same system, eg structural connectivity, morphology and gene expression.

Table 2: Overview of optomechanical components.

Component	Manufacturer	Part#	Specifications
Lasers	Cobolt AB, Sweden	MLD	405nm (for DAPI), 80mW, s-polarised
		MLD	445nm (for CFP), 50mW, s-polarised
		Calypso	491nm (for GFP, FITC), 50mW, s-polarised
		Fandango	515nm (for Venus, YFP), 50mW, s-polarised
		Jive	561nm (for dTomato, PI, RFP), 50mW, s-polarised
AOFT	AA Opto-Electronic, France	AOTFnC-400.650-TN	> 90% diffraction efficiency, 3nm resolution, low cross talk between laser lines, high separation angle
Laser modulator	Qioptiq GmbH, Germany	LM 0202 VIS ADP	400-650nm , $\lambda/2$ -voltage (633nm): 210V
Pulse amplifier	Falco Systems, The Netherlands	WMA-300	50x amplification up to $\pm 150$ V, DC to 5MHz signal bandwidth
Galvo scanner	Cambridge Technology, USA	6220H	small angle step response $200\mu s$
Objectives	Nikon; Japan	Plan Fluor EPI	10x0.3NA, WD 17.5mm, EFL 20mm (excitation)
	Olympus, Japan	LMPLFLN20X	20x0.4NA, WD 12mm, EFL 9mm (detection)
Motor stages	Physik Instrumente, Germany	C-863.11	DC servo-motor controller
		M-122	Travel range 25mm, $0.1\mu m$ resolution, max. velocity 20mm/s
		M-116	Precision Rotation Stage, $2.5\mu rad$ , max. velocity $20^\circ/s$
Camera	Hamamatsu, Japan	Orca Flash4.0	sCMOS sensor, 2048(H) x 2048(V), cell dim.: $6.5\mu m$ , active area: 13.3mm x 13.3mm, 16bit images
DAQ board	National Instruments, USA	NI PCIe-6353	AI: 1 MS/s multichannel; 16-bit resolution, 10 V; AO: 2.86 MS/s, 16-bit resolution, 10 V; digital I/O lines (hardware-timed up to 10 MHz), 100MHz max counter frequency
Workstation	Dell, USA	T7500	12GB RAM, Intel Xeon Processor X5647 @ 2.93 GHz, 64bit OS, Win7

Table 3: Imaging properties and derived quantities. The thickness of the light sheet is approximately of the same size as the depth of field of the high NA detection lens.

Detection			
wavelength	$\lambda$	0.5	$\mu m$
refractive index	$n$	1.45	
numerical aperture	$NA_d$	1	
magnification	$M_{\text{eff}} = f_{\text{TL}}/EFL$	27.8	
tube lens	$f_{\text{TL}}$	200	$mm$
effective focal length objective	$EFL = f_{\text{TL}}/M$	7.2	$mm$
diameter back focal plane	$BFP = 2 \cdot EFL \cdot NA_d$	14.4	$mm$
field number	$FN$	18	$mm$
field size in specimen	$S = FN/M$	0.65	$mm$
depth of field	$\Delta = \lambda \cdot n / (NA_d)^2 + n \cdot e / M \cdot NA_d$	1.06	$\mu m$
Airy radius lat.	$r_A = 0.61\lambda / NA_d$	0.31	$\mu m$
Excitation			
numerical aperture	$NA_e$	0.3	
magnification, nominal	$m$	10	
tube lens	$f_{\text{tl}}$	100	$mm$
effective focal length, objective	$\text{efl} = f_{\text{tl}}/m$	20	$mm$
magnification, effective	$m_e = f_{\text{tl}}/\text{efl}$	5	
refractive index	$\eta$	1	
beam radius	$\omega$	4.5	$mm$
min light sheet waist	$\omega_0 = \lambda \text{efl} / \pi \omega$	1.41	$\mu m$
confocal parameter	$b = 2\pi\omega_0^2/\lambda$	25.15	$\mu m$
Camera			
cell size	$e$	6.5	$\mu m$
effective area	$r^2$	13.3 <sup>2</sup>	$mm^2$
line read out time	$t$	9.7	$\mu s$
line exposure time	$l$	3	$ms$
slit width, camera space	$d_c = l \cdot e / t$	2	$mm$
slit width, sample space	$d_s = d_c / M$	0.72	$mm$
frame rate	$\nu = 1/(2048 \cdot t + l)$	43.6	$Hz$

## Acknowledgments

workshop boys cause they are amazing. Human Brain Project tutta la vita. GARR gave us a beautiful 10gb fiber to cineca CINECA for hosting us on pico

## References

- 1 J. Huiskens and D. Y. Stainier, “Selective plane illumination microscopy techniques in developmental biology,” *Development* **136**(12), 1963-1975 (2009). [1](#)
- 2 K. Chung, J. Wallace, S. Y. Kim, S. Kalyanasundaram, A. S. Andalman, T. J. Davidson and K. Deisseroth, “Structural and molecular interrogation of intact biological systems,” *Nature* **497**(7449), 332-333 (2013). [5](#)
- 3 R. Tomer, L. Ye, B. Hsueh and K. Deisseroth, “Advanced CLARITY for rapid and high-resolution imaging of intact tissues,” *nature protocols* **9**(7), 1682-1697 (2014). [5](#)
- 4 A. Kaufmann, M. Mickoleit, M. Weber and J. Huiskens, “Multilayer mounting enables long-term imaging of zebrafish development in a light sheet microscope,” *Development* **139**(17), 3242-3247 (2012). [5](#)
- 5 P. Pitrone, J. Schindelin, L. Stuyvenberg, S. Preibisch, M. Weber, K. W. Eliceiri, J. Huiskens and P. Tomancak, “OpenSPIM—an open access platform for light sheet microscopy,” *arXiv preprint arXiv:1302.1987*, 3242-3247 (2013). [5](#)
- 6 O. E. Olarte, J. Licea-Rodriguez, J. A. Palero, E. J. Gualda, D. Artigas, J. Mayer and P. Loza-Alvarez, “Image formation by linear and nonlinear digital scanned light-sheet fluorescence microscopy with Gaussian and Bessel beam profiles,” *Biomedical optics express* **3**(7), 1492-1505 (2012). [5](#)
- 7 P. J. Keller and E. H. K. Stelzer, “Quantitative in vivo imaging of entire embryos with digital scanned laser light sheet fluorescence microscopy,” *urr. Opin. Neurobiol.* **18**(6), 624-632 (2008). [4](#)
- 8 P. J. Keller, A. D. Schmidt, J. Wittbrodt, and E. H. K. Stelzer, “Reconstruction of zebrafish early embryonic development by scanned light sheet microscopy,” *Sciences* **322**(5904), 1065-1069 (2010). [4](#)
- 9 E. Baumgart and U. Kubitschek, “Scanned light sheet microscopy with confocal slit detection,” *Optics express* **20**(19), 21805-21814 (2012). [5](#)
- 10 L. Silvestri, A. Bria, L. Sacconi, G. Iannello, and F. S. Pavone, “Confocal light sheet microscopy: micron-scale neuroanatomy of the entire mouse brain,” *Opt Express* **20**(18), 20582-20598 (2012).
- 11 P. Frascioni, L. Silvestri, P. Soda, R. L. Cortini, F. S. Pavone and G. Iannello, “” *Bioinformatics* **30**(), i587-i593 (2014).
- 12 A. Bria and G. Iannello, “TeraStitcher-A tool for fast automatic 3D-stitching of teravoxel-sized microscopy images,” *BMC bioinformatics* **13**(1), 316 (2012). [12](#)
- 13 G. Castagna, “*Object-Oriented Programming A Unified Foundation*,” Birkhäuser, Boston (1997). [7](#)
- 14 I. Costantini, J.-P. Ghobril, A. P. Di Giovanna, A. L. Allegra Mascaro, L. Silvestri, M. C. Muel-lenbroich, L. Onofri, V. Conti, F. Vanzi, L. Sacconi, R. Guerrini, H. Markram, G. Iannello, and F. S. Pavone, *submitted*.

- 15 N. Kovacevic, J. T. Henderson, E. Chan, N. Lifshitz, J. Bishop, A. C. Evans, R. M. Henkelman, and X. J. Chen, "A Three-dimensional MRI Atlas of the Mouse Brain with Estimates of the Average and Variability", *Cereb. Cortex* **15**(5), 639-45 (2005). 10
- 16 P. A. Blume, "*The LabVIEW Style Book (National Instruments Virtual Instrumentation Series)*," Prentice Hall PTR (2007). 8

## List of Figures

- 1 (A) Topview of the excitation path. The galvo scanners are mounted above periscopes. LP: long-pass filter, I: iris, AOTF: acousto-optical tunable filter, LM: laser modulator, PBS: polarisation beam splitter, ABCD: flip mirrors. Inset: detection. (B) Oblique view of the microscope. A custom-made breadboard serves to mount the sample chamber and objectives at an elevated height and features two circular holes at the edges for the periscopes and a large central cut out for the translation stages. A second breadboard is used for the camera.
- 2 Schematic of light sheet microscopy. (A) Fluorescence excitation (along x axis) and detection (along z axis) are operated on independent, perpendicular light paths where the excitation light sheet and the detection focal plane overlap. (B) The custom-made sample chamber is assembled with silicone bellows and seal rings. The clarified, fluorescently-labelled brain is mounted on a Teflon cylinder in the centre of the watertight chamber (C) and can be translated and rotated freely with piezo motors (D). (E) Mounting of a clarified, fluorescently labelled brain. The brain is glued onto a coverslip and inserted into an adapter that slides into the Teflon cylinder.
- 3 Optical characterisation. (A) Exemplary lateral and axial intensity profiles of sub-resolution beads and fits to Gaussian. (B) For each unit 10 bead profiles were fitted in all three dimensions and their FWHM was averaged. (C) The signal to noise ratio.
- 4 Schematic views of the hardware (A) and software (B) architectures of the microscope, showing physical and logical connections, respectively. The software architecture scheme clarifies the hierachic structure of the Murmex components. AO analog output, DO digital output, DI digital input.
- 5 This graph needs a caption.
- 6 Scheme of the data flow. (A) Data streaming on the microscope. SSD: solid-state disk, RAID: redundant array of independent disks, NAS: network-attached storage. (B) Data production rate versus data conversion rate showing the maximum acquisition time and tomography size feasible before the SSD are filled up.
- 7 Whole mouse brain tomography. Imaging of whole transgenic mouse brains treated with CLARITY and cleared with TDE 63% imaged with LSM (Olympus, 25X objective). (A) 3D rendering of a parvalbumin-dTomato brain. (B) 3D rendering of stacks from PV-dTomato mouse brain, GAD-dTomato mouse brain, PI stained mouse brain, FITC-albumin labeled mouse brain, scale bar = 400  $\mu$ m. (C,D,E,F) High resolution insert, of the stack corresponding to red boxes in C. Scale bar = 100  $\mu$ m.



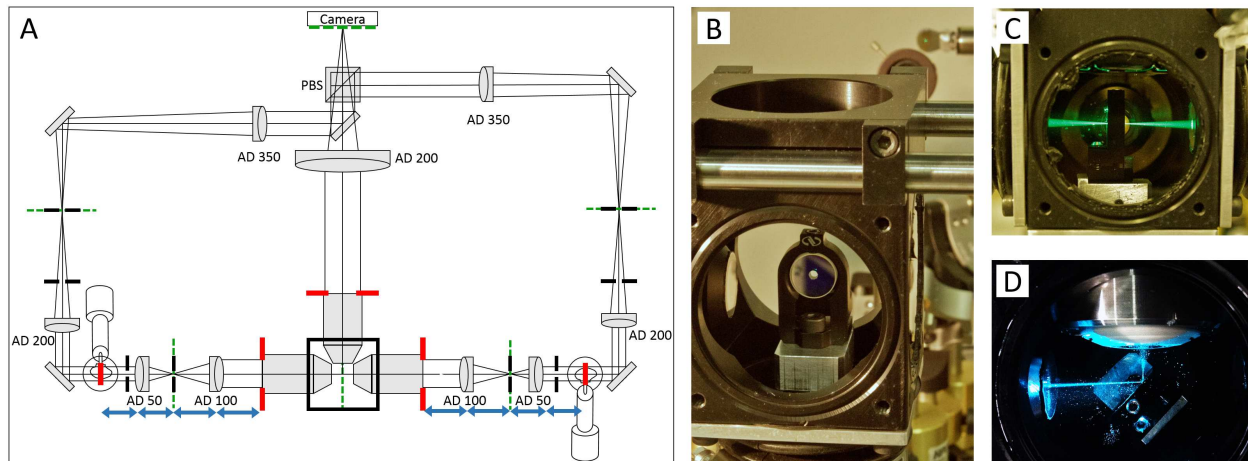


Fig 8: (A) Basic geometrical optics of a double-sided illumination light sheet microscope. AD: achromatic doublet, PBS: polarising beam splitter, red: objective back focal planes and conjugated telecentric planes, green: image planes, blue: 4f telecentric lens system, black: alignment irises. (B) Alignment mirror with drilled hole for light transmission, mount for tip adjustment and adaptor for the Teflon tube. (C) With lateral movement the alignment mirror can be placed such that light is transmitted into the opposing excitation arm. (D) The alignment mirror can be rotated to precisely reflect by  $90^\circ$ .

- 8 (A) Basic geometrical optics of a double-sided illumination light sheet microscope. AD: achromatic doublet, PBS: polarising beam splitter, red: objective back focal planes and conjugated telecentric planes, green: image planes, blue: 4f telecentric lens system, black: alignment irises. (B) Alignment mirror with drilled hole for light transmission, mount for tip adjustment and adaptor for the Teflon tube. (C) With lateral movement the alignment mirror can be placed such that light is transmitted into the opposing excitation arm. (D) The alignment mirror can be rotated to precisely reflect by  $90^\circ$ .
- 9 (A) Working principle of a microscope objective (left): a collimated input beam is converted into a spherical wavefront. Right: inverted light path, a focal spot in the back aperture creates a collimated output. (B) Recursive placement of lenses using the sample mirror in back-reflection mode, (C) in transmission mode and (D) in reflection mode.

## List of Tables

- 1 Data production
- 2 Optomechanics
- 3 Resolution

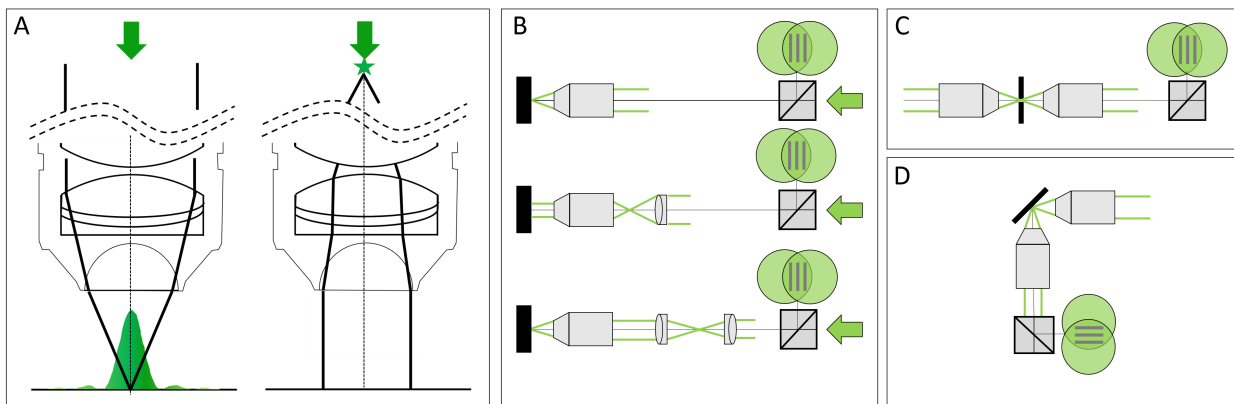


Fig 9: (A) Working principle of a microscope objective (left): a collimated input beam is converted into a spherical wavefront. Right: inverted light path, a focal spot in the back aperture creates a collimated output. (B) Recursive placement of lenses using the sample mirror in back-reflection mode, (C) in transmission mode and (D) in reflection mode.

## 10 Supplementary information

### 10.1 Alignment

For light sheet microscopy it is crucial that excitation and detection occur on perpendicular axes because any deviation from this geometry results in obscured images of reduced resolution and contrast. The objectives need to be perfectly confocal so that the fluorescence that is generated in the swept excitation beam also falls within the detection objective's focal plane. Telecentric imaging, that is the imaging with two lenses which are the sum of their focal lengths apart, a so-called 4f re-imaging system (Figure 8, A), is used to re-image the galvo scanners onto the back apertures of the excitation objectives. In the detection path, the camera chip needs to be positioned in an image plane of the detection objective. Additionally, homogeneous illumination from both sides impose strict symmetry considerations on both illumination arms that have not only to be sufficiently aligned within themselves respectively but function as a pair with recursive dependence.

Our microscope was aligned with two tools, a shear plate to qualitatively assess collimation and a small mirror that can be mounted inside the sample chamber where the sample would usually be. The 0.5in mirror was first pierced with a drill using a ceramic drill bit to produce a hole roughly in its centre of the approximately the same diameter as the excitation beam inside the sample chamber (Figure 8, B). Using a compact single axis adjustable mirror mount (V50-AX, Newport) attached to the Teflon cylinder inside the chamber allows to adjust the pitch of the reflection with the mount and the yaw with the rotation stage while at the same time providing a very space efficient mounting for the pierced 0.5in mirror. With this “sample mirror” three different position can be easily implemented, firstly, back reflection by hitting the reflective surface at  $0^\circ$ , secondly, transmission by laterally displacing the mirror until the light passes through the drilled hole (Figure 8, C), and thirdly, reflection of the light by  $90^\circ$  by precisely turning the mirror mount by  $45^\circ$  using the rotation stage (Figure 8, D).

The excitation objectives are fixed on mounts which allow three dimensional translation plus pitch and yaw adjustment (LP-1A, Newport). In a first alignment step the beam paths of both excitation arms were brought to overlap through irises placed on the breadboard and the optical

bench without any microscope objectives. We found it useful to use two mirrors in each periscope, one vertically mounted and one mounted at  $45^\circ$  for vertical deflection of the incoming beam. In this way full beam steering can be achieved to realign the periscope before hitting the galvo scanner. After this initial alignment the sample mirror was placed with its reflective surface in the centre of the central cut-out of the breadboard. The first excitation objective was placed into the beam path and brought to focus onto the sample mirror which was adjusted to reflect the light back into the same objective through the irises. Using a shear plate and a beam splitter cube the back reflected light was qualitatively adjusted for collimation using translation along the excitation axis of the objective mount (Figure9,B). The sample mirror was then moved laterally to allow the excitation beam to pass through the drilled hole and the second excitation objective was placed (Figure9,C). This time collimation was checked with the light going through both objectives and so their confocal placement was insured. Both excitation arms were then aligned recursively by starting at the putative confocal point between the objectives and placing successively lens after lens in the direction towards the light source, alternating between the two modalities illustrated in Figure9,A. Finally, the sample mirror was positioned in deflection mode and the detection objective was aligned (Figure9,D).